2D/2D Black Phosphorus/Nickel Hydroxide Heterostructures for Promoting Oxygen Evolution via Electronic Structure Modulation and Surface Reconstruction

Jun Mei,* Jing Shang, Tianwei He, Dongchen Qi, Liangzhi Kou, Ting Liao, Aijun Du, and Ziqi Sun*

2D heterostructures provide another exciting opportunity for extending the application of 2D materials in energy conversion and storage devices, due to their flexibility in electronic structure modulations and surface chemistry regulations. Herein, by coupling liquid-exfoliated and mildly oxidized black phosphorus nanosheets (BP-NSs) with wet-chemically synthesized 2D nickel $Ni(OH)_2$ nanosheets (NH-NSs), 2D/2D heterostructured nanosheets (BNHNSs) are rationally constructed with a favorable transition of electron structure and desired intermediate adsorptions for alkaline oxygen evolution reaction (OER) catalysis. When used as an OER catalyst, to reach a current density of 10 mA cm^{-2}, the overpotential of 2D/2D BNHNSs is only 297 mV, corresponding to a considerable decrease of 22% and 34% compared with the individual 2D NH-NSs and 2D BP-NSs, respectively. The structural tracking at the initial reconstruction stage via time-dependent Raman spectra confirms that the phosphorus oxidization into the P–OH and the phase transformation into oxyhydroxide (NiOOH) significantly promote the electron transfer and electrocatalytic efficiency and thus endow the 2D/2D BNHNSs with much enhanced OER catalytic activity. This work offers new insights on the electron structure modulation of 2D-based heterostructures and opens new avenues for regulating the adsorption of emerging phosphorene-based materials for electrocatalysis.

1. Introduction

2D-based heterostructures have demonstrated promising potentials in electrocatalysis for supporting generation and transformation of green fuels, which is primarily due to integrated advantages of each individual 2D unit and unique electron coupling characteristics at the confined 2D/2D interfaces for electrochemical reactions.[1] Electrochemical water splitting,

as one crucial technology for hydrogen production, has received intensive attention in recent years. The current progress, however, is still far away from industrial applications. The major concerns are associated with electrocatalysts, particularly for the half-reaction, oxygen evolution reaction (OER). An ideal catalyst toward OER should manifest a high catalytic efficiency but a low material cost. Compared to the dominate noble-metal-based electrocatalysts, transition metal compounds are expected to be promising candidates to replace noble metals, ascribed to their low production costs and comparable catalytic properties.[2] Among these, nickel (Ni)-based hydroxides have been regarded as one of the most active OER catalysts, particularly in alkaline electrolytes.[3] The catalytic property of the pristine nickel hydroxide ($Ni(OH)_2$), however, is yet far from satisfactory,[4] and further structural or chemical optimization is always demanded for promoting its OER performance. To date, several strategies have been employed for enhancing the catalytic performance of $Ni(OH)_2$ catalyst, including i) manipulating the size or dimensionality for more active sites,[5–7] ii) pairing with other OER-active counterparts for better activity,[8–10] iii) doping with heteroatoms (e.g., Fe, V, W, and Ce) to tailor the electronic structure and surface adsorption behaviors,[11–17] and iv) creating defective surfaces or interfaces.[18–20] Despite that significant efforts in regulating morphologies and/or structures have been undertaken, new

J. Mei, D. Qi, A. Du, Z. Sun
School of Chemistry and Physics
Queensland University of Technology
2 George Street, Brisbane, QLD 4000, Australia
E-mail: j2.mei@qut.edu.au; ziqi.sun@qut.edu.au

J. Mei, D. Qi, L. Kou, T. Liao, A. Du, Z. Sun
Centre for Materials Science
Queensland University of Technology
2 George Street, Brisbane, QLD 4000, Australia

J. Shang, L. Kou, T. Liao
School of Mechanical
Medical & Process Engineering
Queensland University of Technology
2 George Street, Brisbane, QLD 4000, Australia

T. He
Fritz-Haber-Institut der Max-Planck-Gesellschaft
Faradayweg 4-6, 14195 Berlin, Germany

optimization strategies, aiming to modulate the electronic structure for achieving the desired adsorption of the reaction intermediates, are highly required for promoting the OER activity of 2D nickel Ni(OH)$_2$ nanosheets (NH-NSs).

As one of the emerging 2D nanomaterials, black phosphorus (BP) nanosheets (BP-NSs) possess some unique properties, such as high charge-carrier mobility and tunable bandgap,[21] which are highly desired in applications such as electrode materials or catalysts for energy conversion and storages, including rechargeable batteries and electrocatalysis.[22–24] Compared with bulk-form BP, 2D BP-NSs provide much more active sites on the ultrathin planar structure, which can dramatically enhance the electrocatalytic activities.[25] Despite these promising physical characteristics endowing the pristine 2D BP-NS as an ideal electrocatalyst, it has been recognized that an excessive adsorption energy toward oxygen-containing intermediates is needed during OER catalysis, and thus leads to large OER overpotentials.[26] To address this intrinsic issue, many effective solutions have been proposed for optimizing the intermediate adsorption on the 2D BP-NSs, such as heterostructuring with non-metal counterparts (e.g., N-doped graphene and graphitic carbon nitride),[27,28] pairing with metal phosphides (e.g., Co$_2$P),[29] coupling with amorphous metal oxides (e.g., CoFe-O),[30] compositing with amorphous metal borides (e.g., CoFeB) nanosheets,[31] and hybridizing with metal nanoparticles (e.g., Au and Co).[32,33] In spite of achieved great progress, further efforts on modulating the electronic structure to achieve nearly thermo-neutral intermediate adsorption are yet undergoing for improving the OER performance of 2D BP-NSs.

Herein, 2D/2D heterostructured nanosheets (BNHNSs) with a favorable electronic structure transition toward an ideal intermediate adsorption for alkaline OER are rationally designed by coupling the liquid-exfoliated 2D BP-NSs with the wet-chemically synthesized 2D NH-NSs. The rational combination of 2D BP-NSs with 2D NH-NSs can compensate the drawbacks of each 2D unit and promote the synergetic effect. Furthermore, this can induce strong interfacial coupling at the heterostructure, which results in optimized electron transfer and surface adsorption behaviors to address the intrinsic drawbacks of each individual 2D unit. This novel 2D/2D heterostructure manifests undesired adsorption of the oxygen-containing intermediates during alkaline OER catalysis, as demonstrated by both theoretical calculation and experimental validation. By tracking the structural reconstruction at the initial stage, the formation of P–OH surface oxidizing groups and a crucial transformation of Ni sites into nickel oxyhydroxide (NiOOH) on the surface provide abundant real active sites for sustaining continuous cycles. This heterostructure design opens a new approach to further optimize the properties of 2D BP-NSs for promoting their catalytic activity and offers some critical insights into the surface catalytic mechanisms of 2D/2D heterostructures in electrocatalysis.

2. Results and Discussion

Van der Waals (vdW) bonded 2D/2D BNHNSs proposed in this work were synthesized by assembly of the individually fabricated 2D NH-NSs and 2D BP-NSs. As illustrated in **Figure 1**a,

the well-dispersed mildly oxidized 2D BP-NSs were obtained by liquid exfoliating bulk-form of BP and the 2D NH-NSs were synthesized via a wet-chemical method from nickel nitrate hexahydrate (Ni(NO$_3$)$_2$ 6H$_2$O) precursor and sodium acetate trihydrate (CH$_3$COONa 3H$_2$O) PH-adjusting agent. The 2D dispersions were mixed with desired amount and then dip-coated onto a carbon cloth (CC) substrate. After drying in vacuum, 2D/2D BNHNSs loaded onto CC electrodes were finally obtained. X-ray diffraction (XRD) characterizations confirmed the successful fabrication of the 2D units. As shown in Figure 1b, typical peaks located at 14.3°, 29.2°, and 38.0° corresponding to the (020), (021), and (040) planes of BP were identified and a strong preferred orientation perpendicular to the (010) of the BP nanosheets appeared resulted by the alignment of nanosheets with the substrate.[34] For the 2D NH-NSs, three peaks at 19.2°, 38.5°, and 52.1° were assigned to the (001), (101), and (102) planes of a hexagonal β-Ni(OH)$_2$ structure with the lattice constants of $a = b = 0.3126$ and $c = 0.4605$ nm (JCPDS No. 14–0117).[35] Owing to the 2D feature, a preferred orientation of (001) was observed. The appearance of preferred orientation is strong evidence of the successful fabrication of 2D nanosheets.

Transmission electron microscope (TEM) and atomic force microscope (AFM) were used to examine the 2D morphologies and the sheet thicknesses of 2D NH-NSs and 2D BP-NSs. For the as-synthesized 2D NH-NSs, a planar size up to hundreds of nanometers was clearly identified (Figure 1c and Figure S1, Supporting Information). The lattice fringe of 0.23 nm (Figure 1d) is well consistent to the d-spacing of the (101) plane of Ni(OH)$_2$. As identified by AFM (Figure 1e), the thickness of the 2D NH-NSs was around 10 nm, and the relatively rough surface of 2D NH-NSs suggested the existence of mild oxidization. As for the BP-NSs, the 2D sheet-like morphology (Figure 1f and Figure S2, Supporting Information) with a lattice fringe of 0.22 nm (Figure 1g) and a thickness of 2.9 nm (Figure 1h) were observed, indicating the successful exfoliation of the 2D sheets from the bulk crystals.[36] After mixing the dispersions of both 2D NH-NSs and BP-NSs, 2D/2D BNHNSs were dip-coated onto the CC substrate, as evidenced by the field-emission scanning electron microscope (FE-SEM) image and the elemental mapping with a uniform element distribution of C, O, Ni, and P of the 2D/2D heterostructure (Figure 1i–m). Furthermore, the co-existence of the lattice fringes in the TEM image and the Ni/P elements in the mapping patterns confirmed the successful formation of 2D/2D BNHNSs (Figure S3, Supporting Information). For the purpose of comparison, individual 2D NH-NSs (Figure S4, Supporting Information) and individual 2D BP-NSs were also dip-coated onto the CC substrate for the following OER measurements.

Crystal chemistry of the as-prepared 2D NH-NSs, 2D BP-NSs, and 2D/2D BNHNSs were evaluated by Raman, X-ray photoelectron spectroscopy (XPS), and Near-edge X-ray absorption fine structures (NEXAFS) measurements. In the Raman spectra (**Figure 2**a), three representative modes located at 314, 448, and 3580 cm^{-1} of the 2D NH-NSs agree well with the reported characteristic resonances of β-Ni(OH)$_2$.[37] For 2D BP-NSs, three obvious peaks located at 363, 440, and 468 cm^{-1} can be assigned to the characteristic A$_g^1$, B$_{2g}$, and A$_g^2$ models of BP, respectively.[38] The appearance of major Raman characteristic peaks demonstrates that the crystal structure

**ADVANCED
SCIENCE NEWS**

www.advancedsciencenews.com

**ADVANCED
ENERGY
MATERIALS**
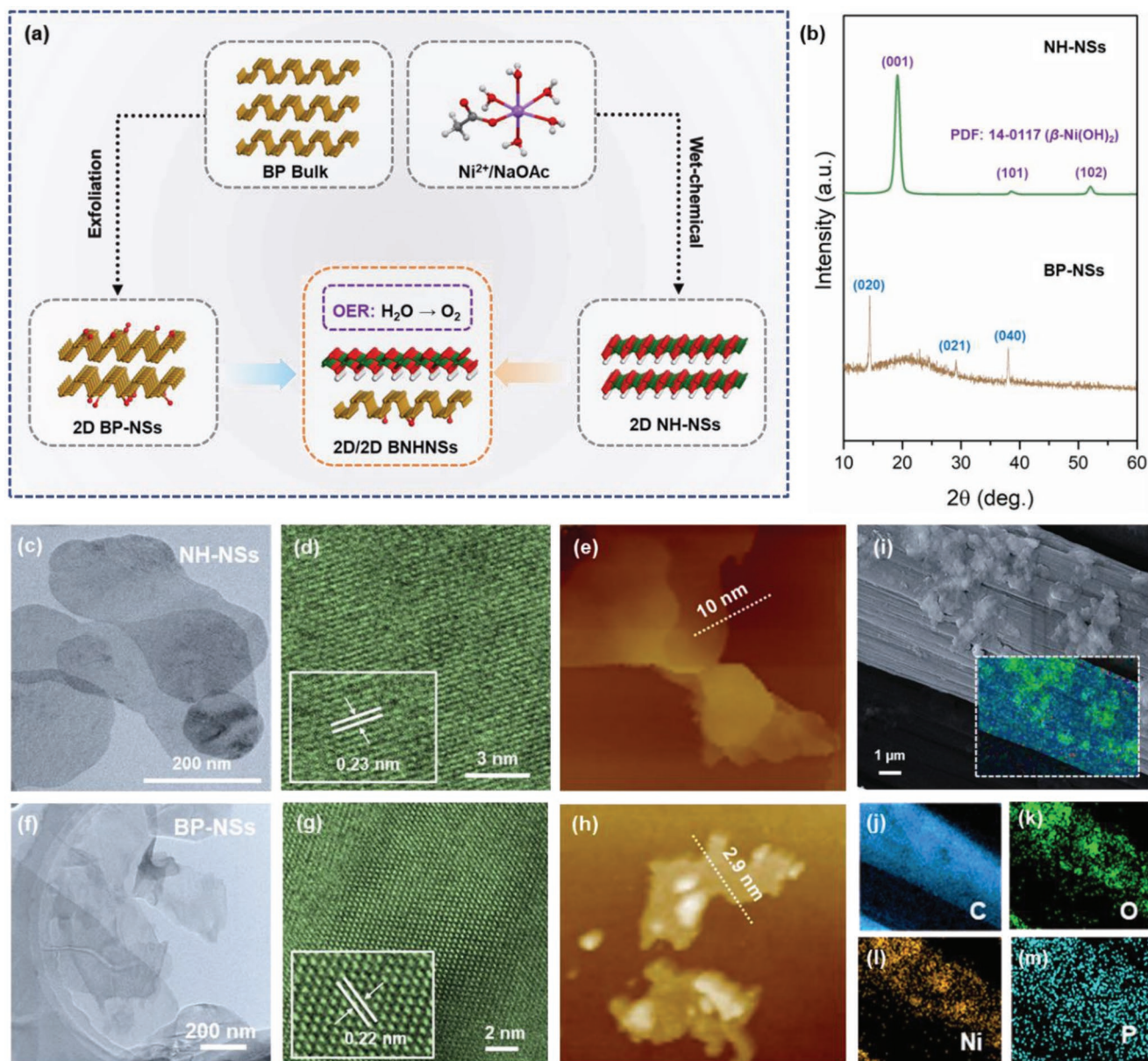
www.advenergymat.de

Figure 1. a) Schematic illustration of synthesis of 2D/2D heterostructured nanosheets (BNHNSs) by coupling 2D Ni(OH)$_2$ nanosheets (NH-NSs) and 2D black phosphorus (BP) nanosheets (BP-NSs). b) XRD patterns of the as-prepared 2D NH-NSs and 2D BP-NSs. c) Low-magnification and d) high-magnification TEM images, and e) AFM image of the as-prepared 2D NH-NSs. f) Low-magnification and g) high-magnification TEM images, and h) AFM image of the as-prepared 2D BP-NSs. i) SEM image of the 2D/2D BNHNSs loaded onto CC and j–m) the corresponding element mapping patterns of C, O, Ni, and P.

2D forms of both BP-NSs and NH-NSs have not undergone significant change or distortion. After combination into the 2D/2D BNHNSs, both Raman signals belonging to 2D NH-NSs and 2D BP-NSs could be identified, indicating the co-existence of both 2D units (Figure S5, Supporting Information). XPS provides more refinement information on the chemical states of the surface atoms. As shown in the Ni 2p spectra in Figure 2b, a pair of sharp peaks assigned to the Ni 2p$_{3/2}$ (855.26 eV) and Ni 2p$_{1/2}$ (872.87 eV) spin orbit levels suggested the existence of a Ni(II) state in the 2D NH-NSs. In the fitted P 2p spectra of the 2D BP-NSs (Figure 2c), a couple of peaks located at 129.6 eV (P 2p$_{3/2}$) and 130.3 eV (P 2p$_{1/2}$) should originate from

elementary P^0, demonstrating the presence of BPNs. Another two peaks at higher binding energies at 131.1 and 133.3 eV should be attributed to the adsorbed oxygen and the P–O species, respectively, which were caused by mild oxidization.[39]

To further reveal the structural vibrations at a more accurate way, NEXAFS were performed to examine the P K-edge, O K-edge, and Ni L-edge for the 2D BP-NSs, the 2D NH-NSs, and the 2D/2D BNHNSs. In the Ni L-edge spectra of 2D-NH-NSs, four characteristic peaks at 853.0, 855.1, 870.0, and 871.3 eV appeared (Figure 2d), corresponding to the typical β-Ni(OH)$_2$ structure.[40,41] After assembled into 2D/2D BNHNSs, no obvious change on the Ni coordination was observed. In the P K-edge
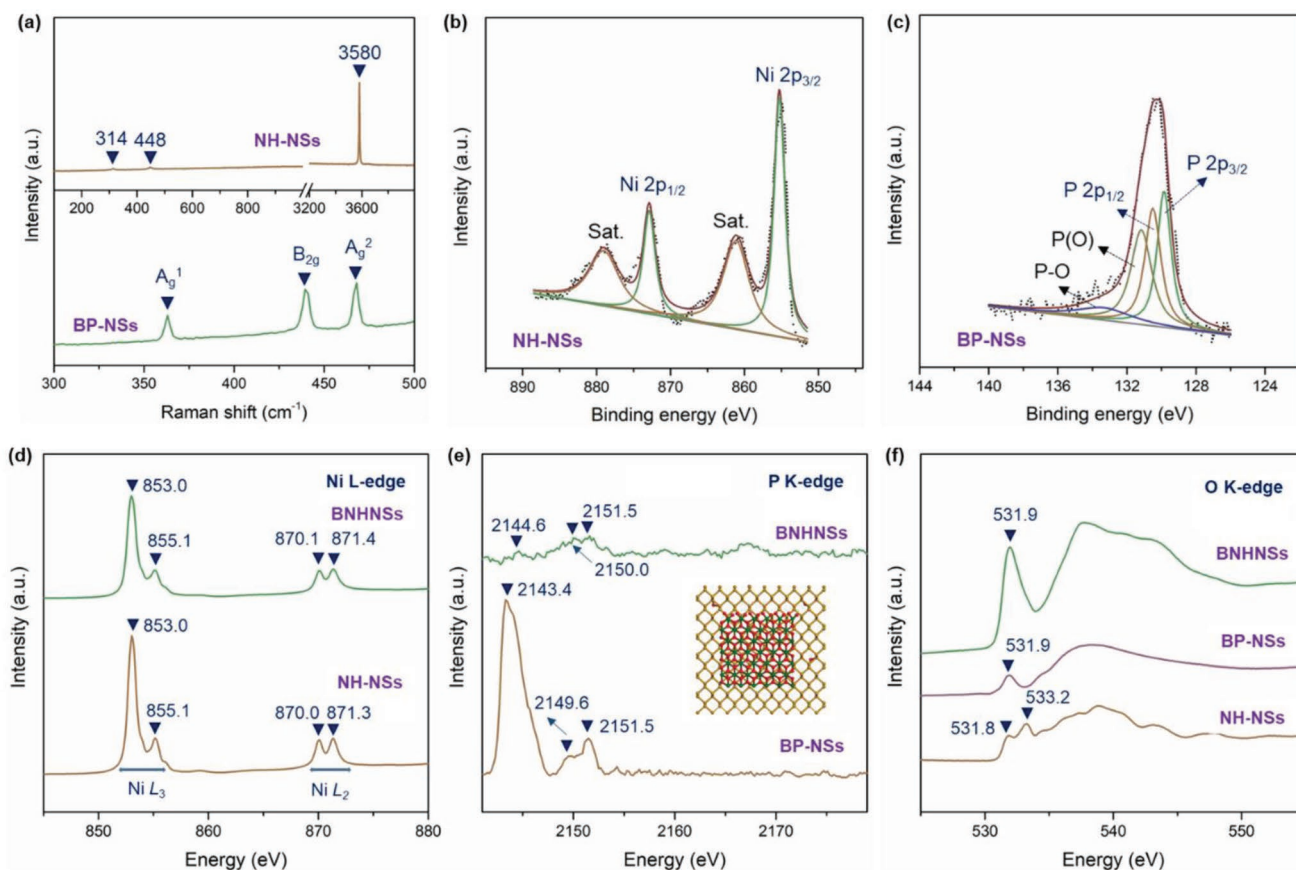
Figure 2. a) Raman spectra of the as-prepared 2D NH-NSs and 2D BP-NSs. b) High-resolution Ni 2p spectra of the as-prepared 2D NH-NSs. c) High-resolution P 2p spectra of the as-prepared 2D BP-NSs. d–f) NEXAFS comparisons at d) Ni L-edge, e) O K-edge, and f) P K-edge of the as-prepared 2D NH-NSs, 2D BP-NSs, and 2D/2D BNHNSs.

spectrum of the 2D BP-NSs (Figure 2e), a typical sharp peak for phosphorus was found at 2143.4 eV, and some peaks at higher energies over 2147 eV verify the presence of P–O bonding interaction. Compared with 2D BP-NSs, these P K-edge peaks in the 2D/2D BNHNSs became inapparent, due to the overlapping stack of 2D NH-NSs and 2D BP-NSs, and manifest higher photon energies (Figure 2e) possibly aroused by the charge transfer process from the phosphorus atoms to other atoms.[42] Furthermore, with the comparison on the O K-edge spectra of 2D NH-NSs, 2D BP-NSs, and 2D/2D BNHNSs (Figure 2f), it could be concluded that the chemical environment of oxygen was affected after assembled into 2D/2D heterostructures, suggesting the possible existence of P–O–Ni/C bonding for coupling the surface-active 2D NH-NSs with the partially oxidized 2D BP-NSs.

As we previously discussed, the vdW bonded 2D/2D heterostructures have not strong interferences on the crystal structure of constituent materials but can alter the electronic structures and the localized surface chemistry, which can bring significant impact to the interface charge and mass transport, the chemical coordination of surface reactive centers, and the surface intermediate adsorptions behaviors and activities. Based on the above characterizations, it is clear that the 2D/2D BNHNSs are a type of vdW heterostructure and should present different catalytic performance compared with the individual 2D materials. For the proof of the concept, electrocatalytic OER properties were

evaluated on the 2D NH-NSs, 2D BP-NSs, and 2D/2D BNHNSs loaded CC working electrodes in a 1.0 M KOH solution. As compared in **Figure 3**a for linear sweep voltammetry (LSV) curves, at a constant overpotential of 400 mV, the limiting density for 2D/2D BNHNSs was over 100 mA cm^{-2}, which is nearly tenfold increase compared to that of 2D NH-NSs ($\approx$12 mA cm^{-2}) and RuO$_2$ benchmark. Further comparison on the Tafel curves concludes that the resulting 2D/2D BNHNSs delivered the lowest slope, showing the fastest reaction kinetic (Figure S6, Supporting Information). At a current density of 10 mA cm^{-2}, the overpotentials for 2D NH-NSs and 2D BP-NSs were over 380 and 450 mV, respectively, indicating the weak OER activity. When assembled into 2D/2D BNHNSs, only 297 mV was required to reach 10 mA cm^{-2} under the same conditions. If the current density increased from 10 to 50 mA cm^{-2}, only 22% overpotential increase was needed for 2D/2D BNHNSs, which is much lower than that for 2D NH-NSs ($\approx$37%), while the 2D BP-NSs could not reach 25 mA cm^{-2} in the examined potential range (Figure 3b). Compared to some reported BP- and Ni-based electrocatalysts,[26,43] such as N-BP-QDs,[44] BP/Co$_2$P,[29] Co/BP,[32] NiCo$_2$O$_4$,[45] NiCo-LDH,[46] and BP QDs/MXene,[47] the 2D/2D BNHNSs exhibited the lowest overpotential to reach 10 mA cm^{-2} and showed the greatest potential as an efficient catalyst toward OER (Figure 3d and Table S1, Supporting Information). The stability of the 2D/2D BNHNSs was monitored
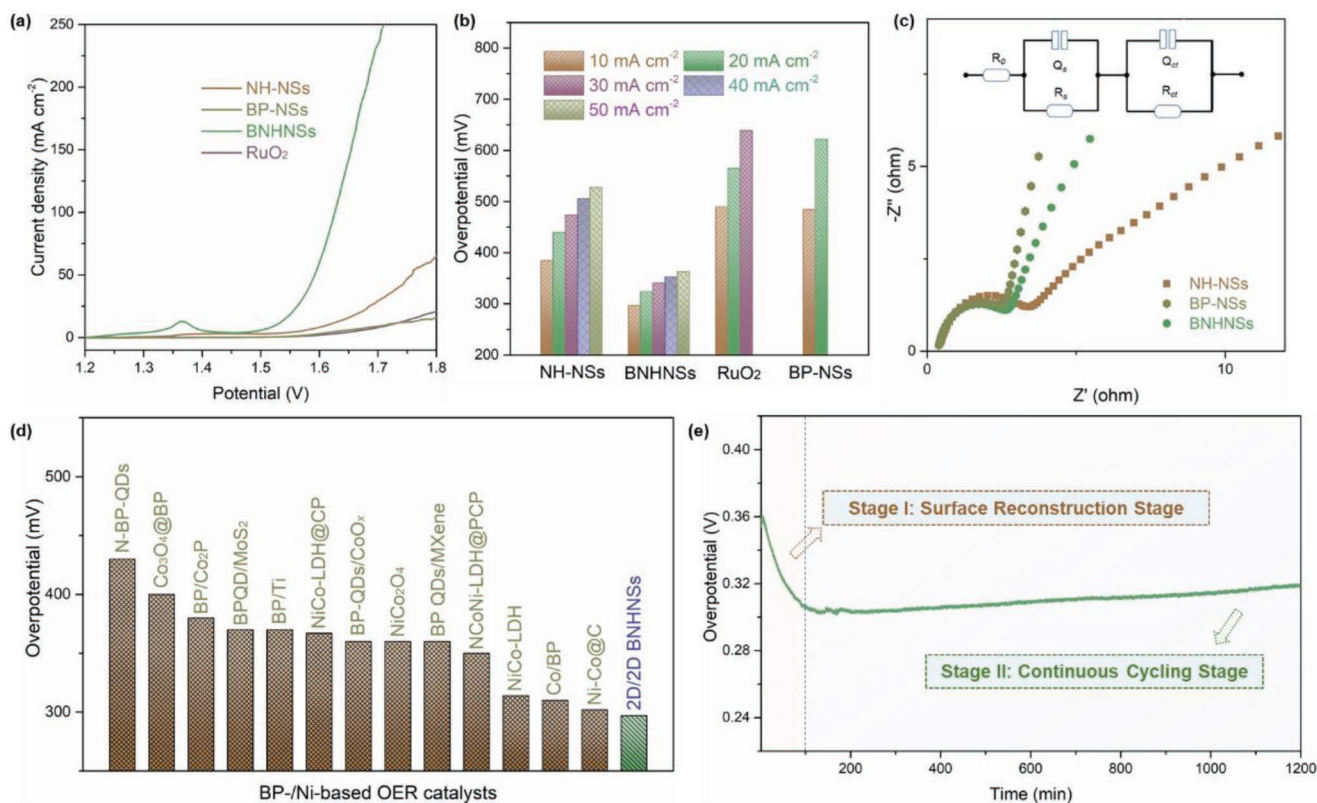
**ADVANCED
SCIENCE NEWS**
www.advancedsciencenews.com

**ADVANCED
ENERGY
MATERIALS**
www.advenergymat.de

Figure 3. a) IR-corrected LSV polarization curves for OER in 1.0 M KOH solution in a potential range of 1.2–1.8 V. b) Comparison of overpotentials at different current densities in the range of 10–50 mA cm^{-2}. c) EIS plots of as-prepared 2D NH-NSs, 2D BP-NSs, and 2D/2D BNHNSs catalysts. Inset shows the equivalent circuit for EIS data fitting. d) Comparison of overpotentials with these reported electrocatalysts at 10 mA cm^{-2}. e) Time-dependent overpotential curves of the 2D/2D BNHNSs catalyst in KOH for 1200 min.

at 10 mA cm^{-2} by using the chronoamperometry technique (Figure 3e). After an initial activation period associated with a drop of overpotential from 360 to 297 mV (Stage I), a stable OER operation was recorded to 1200 min (Stage II), accompanied by a slightly overpotential increase to 320 mV. The enhanced OER performance of the 2D/2D BNHNSs should be largely contributed by the increased active sites, which is one of the major advantages for 2D-based heterostructures for electrocatalysis.[1] To elucidate these, the cyclic voltammetry technique (Figure S7, Supporting Information) was used to calculate the double layer capacitance (C_{dl}), an indicator of electrochemical active surface area (ECSA). Compared with the 2D BP-NSs (≈0.019 cm^{-2}), the resultant 2D/2D BNHNSs (≈0.04 cm^{-2}) delivers a two-fold increase on the ECSA (Figure S8, Supporting Information). Additionally, comparing with the 2D NH-NSs having slow electron transfer as other hydroxides, the 2D/2D BNHNSs presented favorable electron transfer, as verified by the reduced charge transfer resistance (R_{ct}) (≈3.5 Ω for 2D NH-NSs and ≈2.7 Ω for 2D/2D BNHNSs) in the electrochemical impedance spectra (EIS) (Figure 3c). All these results evidence that the 2D/2D BNHNSs manifest the advantages of increased active sites and enhanced electron transfer, which then result in improved reaction kinetic, expanded limiting current densities, and greatly reduced overpotentials, compared with the individual 2D BP-NSs and 2D NH-NSs.

As we observed in the stability test, there was an obvious activation period within the initial 100–120 min (Stage I, Figure 3e),

which brings a significant drop of overpotential from 360 to 297 mV (17.5% enhancement) for maintaining the current density of 10 mV cm^{-2}. To explore the possible mechanism of the initial surface reconstruction stage of the 2D/2D BNHNSs and meanwhile identify the specific roles of each 2D unit during OER, SEM, Raman, and XPS analysis were conducted for exploring the morphological and structural vibrations upon OER cycling within the first 120 min in 1.0 M KOH solution. To exclude the possible effect from CC on electrode characterizations, the working electrodes were prepared by loading the 2D/2D BNHNSs on a polished glass carbon electrode with the presence of the 5% Nafion binder. As shown in **Figure 4**a, as the increase of cycling time, the surfaces of the 2D/2D BNHNSs electrode became rougher and were accompanied with the appearance of fine particles. The EDS mapping demonstrated that the loss of phosphorus was observed in the first 30 min, resulting in the increase of Ni/P ratio from 13 to 14. With the prolong of the cycling from 30 to 120 min, Ni intended to loss and decrease of Ni/P ratio from 11.3 to 7.2 was identified. The variation of the surface elemental distribution indicates that the surface has undergone a sort of structural reorganization, as reported in some oxide/hydroxide electrocatalysts.[48,49]

To monitor the surface changes, time-dependent Raman spectra of the 2D/2D BNHNSs were collected during OER cycles from 5 to 120 min at a current density of 10 mA cm^{-2} in the alkaline solution. Upon cycling, two obvious Raman peaks located at ≈480 and ≈550 cm^{-1} appeared (Figure 4b), which are the representative band couples of γ-NiOOH.[50] Specifically, the
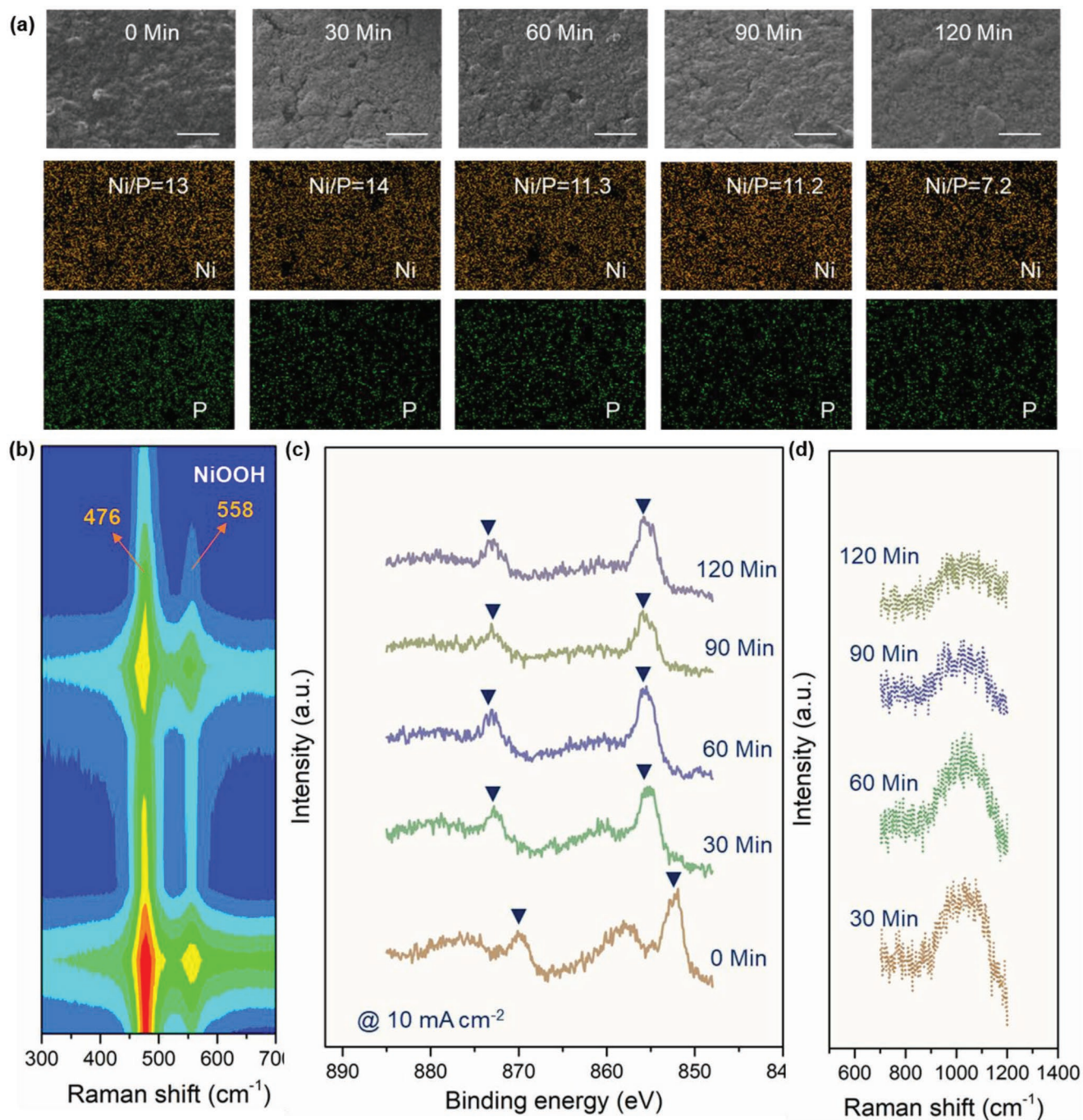
Figure 4. a) SEM images and the corresponding element mapping patterns of Ni and P on the surfaces of the 2D/2D BNHNSs under different intervals at a current density of 10 mA cm^{-2}. Scale bar: 25 µm. b) Time-dependent Raman spectra of 2D/2D BNHNSs among the cycling in the initial 120 min. c) High-resolution XPS spectra of Ni 2p of the 2D/2D BNHNSs catalyst over cycling. d) Raman spectra of 2D/2D BNHNSs catalyst showing the oxidized phosphorus or superoxidic species.

peak at lower wavenumber can be assigned to the depolarized E$_g$ mode (the bending band) and the higher wavenumber peak is contributed by the polarized A$_{1g}$ mode (the stretching band).[51] These results clearly indicate a pre-oxidization process from the initial Ni(OH)$_2$ to the NiOOH upon OER cycling, which acts as the real active site for supporting continuous cycles. This can be further verified by the ex situ XPS analysis

on the Ni 2p state, as shown in Figure 4c. Compared with the fresh 2D/2D BNHNSs, an apparent peak shift of ≈3 eV toward higher binding energies was identified after a cycling time of 30 min, suggesting that an oxidization process occurred to drive the transfer of hydroxide into oxyhydroxide. Combined with the previous reports, the γ-NiOOH phase has an interlayer spacing of ≈7 Å and facilitates the intercalation of water or

ions in-between the layers in the alkaline solution, which can significantly enhance the efficient evolution of oxygen.[52–54] Additionally, a broad band was detected between 850 and 1200 cm^{-1} in the Raman spectra upon cycling (Figure 4d). There might be two primary origins, the generation of superoxidic species (O–O^{-}) in the oxyhydroxide structure (NiOO^{-})[55,56] and the oxidization of phosphorus species (H$_x$PO$_y$, P$_x$O$_y$).[57,58] Combining the surface structural analysis on the 2D/2D BNHNSs electrocatalyst, it is sure that a critical surface reconstruction occurred in the initial 120 min, which activated the surface for much favorable catalytic reactions toward OER. It can be concluded that the Ni sites are crucial for sustaining the OER catalytic performance, and the initial Ni(OH)$_2$ to the NiOOH occurs at the initial cycling stage significantly contributing to the drop of overpotential of the heterostructured catalyst. On the other hand, the loss of P at the beginning should be resulted by the mild oxidation of BP, which allows the existence of hydroxide group on the surface for a thermally optimized adsorption of intermediates. The structural reconstruction resulted by the formation of active NiOOH sites and P–OH sites should be the origin of the significant activation within the initial 120 min.

Theoretical calculations were employed to illustrate the electron coupling effect within 2D/2D BNHNSs and examine the adsorption behaviors of oxygen-containing intermediates during OER. The unique function of the oxidized 2D BP-NSs was revealed by studying effects of the degree of the surface oxidation on the electron structure and the intermediate adsorption behaviors during OER. As mentioned above, the pristine 2D BP-NSs exhibit an unsatisfactory OER performance due to the excessive adsorption toward oxygen-containing intermediates, which leads to a large overpotential during the rate-determining step (RDS, *O → *OOH). As the gradual increase of the oxidation degree, which was realized by the increased oxygen concentration in the 2D BP-NSs models (Figures S9–S12, Supporting Information), the RDSs remained unchanged. However, the overpotentials at the RDSs were reduced (Figure S13, Supporting Information), which is primarily ascribed to the decreased adsorption energy toward the intermediate. Furthermore, as the oxidation level increases, the bandgap of the 2D BP-NSs gradually narrowed from around 1 to 0.3 eV as shown in the density of states (DOS) (Figure S14, Supporting Information), which is much favorable for promoting electron transfer during electrocatalysis. Therefore, during OER cycles, although 2D BP-NSs presented partial oxidation at the initial surface reconstruction stage, it is beneficial to optimizing the electron structure and electrocatalytic intermediate adsorption.

For the 2D NH-NSs exposed with a dehydrogenate surface, the states crossing the Fermi level through the spin-up channel were obviously identified (**Figure 5**a), suggesting a half-metallic
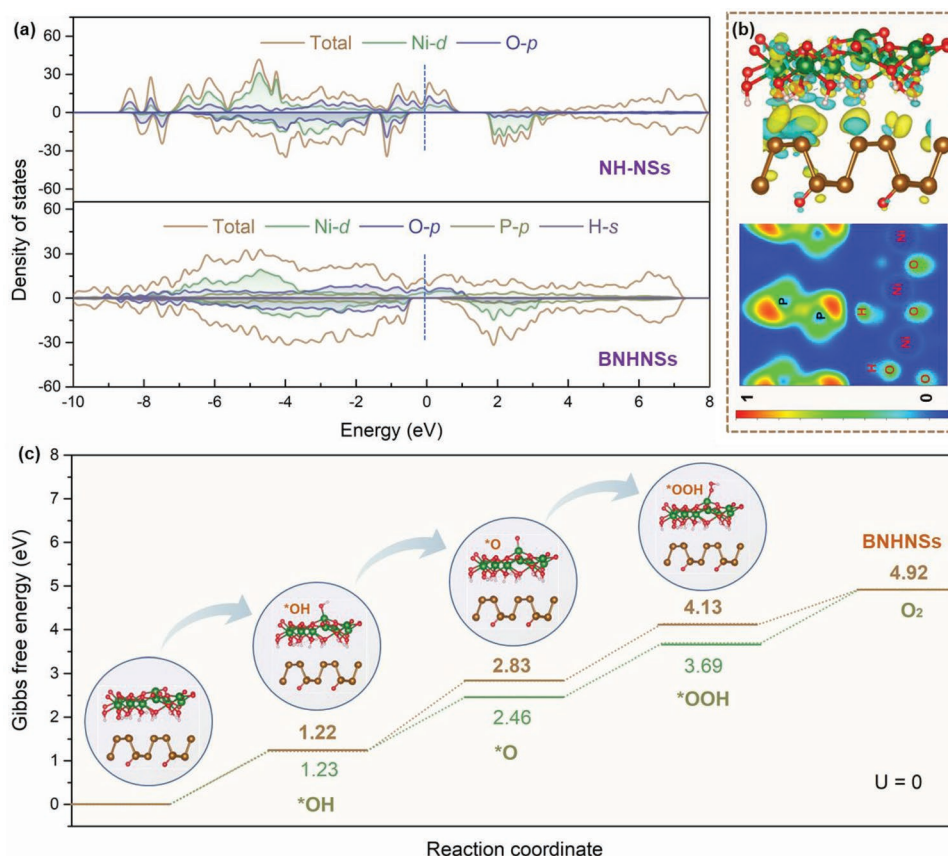

Figure 5. a) Density of states (DOS) of (top) 2D NH-NSs and (bottom) 2D/2D BNHNSs. b) (top) Charge density difference (CDD) and (bottom) electron localization function (ELF) maps of 2D/2D BNHNSs. Yellow and cyan iso-surfaces represent charge accumulation and depletion, and the iso-surface value is 0.001 Å^{-3}. c) Calculated free energy profiles for OER of 2D/2D BNHNSs (brown line) at the U = 0 V as compared with the ideal OER catalyst (green line). Insets show the optimized structures with the adsorption of oxygen-containing intermediates during OER.

characteristic.[59] When the 2D BP-NSs and the 2D NH-NSs are assembled into the 2D/2D BNHNSs heterostructure, the half-metallic characteristic is inherited into the heterostructure with even higher density, which is expected to further contribute to the fastest electron transfer during OER in comparison with the individual 2D BP-NSs and 2D NH-NSs. Partial density of states (PDOS) analysis confirms the spin-up DOS is more contributed by Ni-d and O-p orbitals from 2D NH-NSs. The charge density difference (CDD) and electron localization function (ELF) maps verify the interfacial charge transfer of the heterostructure, in which about 0.23 electrons transferred from the 2D NH-NSs to the 2D BP-NSs over the heterostructured interfaces (Figure 5b). Specifically, the phosphorus atoms in 2D BP-NSs act as the electron donor with a loss of 2.44 electrons. However, the oxygen atoms in the 2D BP-NSs received 2.67 electrons, endowing the mildly oxidized BP-NSs as an electron acceptor. Finally, the OER catalytic reaction pathways on the heterostructure surface were examined. As shown in the calculated free energy profiles of the 2D/2D BNHNSs for alkaline OER (Figure 5c), the overall pathway is close to the ideal case, in which an external potential of 1.23 V was required to ensure the spontaneous progress of each step. These results indicate that the 2D/2D BNHNSs demonstrated almost thermos-neutral intermediate adsorption behaviors toward oxygen-containing intermediates during OER. As summarized, surface reconstruction acts as a crucial role on electronic structure modulation by inducing the phase transitions of nickel hydroxide from the semiconducting hydroxide to the half-metallic oxyhydroxide and the mildly oxidized phosphorus for narrowing bandgap. As a result, the optimized electronic structure is favorable for achieving the ideal adsorption on the oxygen-containing intermediate, endowing them as promising alkaline OER electrocatalysts.

3. Conclusion

To summarize, by coupling the mildly oxidized 2D BP-NSs and the wet-chemically synthesized 2D NH-NSs, a type of vdW bonded 2D/2D BNHNSs was fabricated with modulated electronic structures, optimized surface adsorption behaviors, and enhanced interfacial electron transfer, which significantly promoted the alkaline OER performance. As verified by theoretical calculations and experimental validations, the surface oxidization of 2D BP-NSs into P–OH and the phase transition of 2D NH-NSs into NiOOH oxyhydroxide occurred at the initial reconstruction stage were the origins of new active centers for OER catalysis. This initial surface structural reconstruction greatly reduced the overpotentials and accelerated the kinetics for OER. This work sheds some new insights into the critical roles of initial surface reconstruction onto the catalytic activity and paves a way to the design of electrocatalysis based on 2D/2D heterostructures with proper electronic structure engineering.

4. Experimental Section

Preparation of 2D Nickel Hydroxide (Ni(OH)$_2$) Nanosheets (NH-NSs): Typically, 0.58 g nickel (II) nitrate hexahydrate (Ni(NO$_3$)$_2$ 6H$_2$O, ≥ 97%, Sigma-Aldrich) was dissolved into a water–ethanol mixture consisting of 1.4 mL ultra-pure water (obtained through a PURELAB Maxima purification system) and 20 mL ethanol (Absolute, Ajax Finechem). Then, 1.6 g sodium acetate trihydrate (CH$_3$COONa 3H$_2$O, AR grade, Chem-Supply) was added into the mixture. After being completely dissolved, the mixture was transferred into a sealed hydrothermal autoclave (4744 Vessel, Parr Instrument) and maintained at 180 °C for 12 h. Finally, the NH-NSs powder was collected after centrifugation, washing by water/ethanol, and air-drying for 12 h.

Preparation of 2D Black Phosphorus Nanosheets: Bulk BP crystals (15 mg, Nanjing XFNANO Materials Tech Co., Ltd.) were grinded in a glove box and then added into a glass vial filled with acetone (Ajax Finechem, AR grade, 30 mL). After being bubbled by high-purity nitrogen for 30 min, the sealed vial was transferred into an ultrasonic machine (240 W, VEVOR) and continuously treated for 70 min. After centrifugal separation to remove the bottom precipitate, the BP-NSs dispersion was finally obtained.

Preparation of 2D/2D Heterostructured Nanosheets (BNHNSs): The as-synthesized 2D NH-NSs (10 mg) were dispersed into water (2 mL) under ultrasonic treatment for 60 min to produce 2D NH-NS dispersion (SSN). Then, 5 mL of the as-prepared BP-NS dispersion was added and homogeneously mixed under ultrasonic treatment for another 20 min. Subsequently, 100 µL of the resultant mixture was loaded onto a piece of carbon cloth (CC, 2 × 2 cm), which was finally dried at 40 °C for 5 h under vacuum to obtain the 2D/2D BNHNSs.

Material Characterizations: X-ray diffraction (XRD, Rigaku SmartLab diffractometer, Cu radiation) was used to examine the crystal structure of the as-prepared 2D NH-NSs and 2D BP-NSs. Transmission electron microscope (TEM, JEOL 2100, 200 kV) was used to reveal the morphological and structural details of the as-prepared 2D NH-NSs and 2D BP-NSs. FE-SEM (Zeiss Sigma VP), equipped with an X-ray detector accessory (Oxford XMax), was employed to confirm the loading states and element mapping patterns of the CC samples loaded with 2D NH-NSs, 2D BP-NSs, or 2D/2D BNHNSs. AFM (Bruker Icon Dimension) was applied to check the thickness of the as-prepared 2D NH-NSs or 2D BP-NSs. Raman microscope (Renishaw inVia) was used to collect Raman spectra of the as-synthesized 2D NH-NSs and 2D BP-NSs by using a 532 nm excitation. XPS (Kratos AXIS Supra) analysis with C 1s correction (284.6 eV) was performed on the chemical states of nickel in the 2D NH-NSs and phosphorus in the 2D BP-NSs. NEXAFS at the P K-edge, O K-edge, or Ni L-edge for 2D BP-NSs, 2D NH-NSs, or 2D/2D BNHNSs were obtained at the Soft X-ray Spectroscopy Beamline of Australian Synchrotron (ANSTO).

Supporting Information

Supporting Information is available from the Wiley Online Library or from the author.

**ADVANCED
ENERGY
MATERIALS**

www.advenergymat.de

Conflict of Interest

The authors declare no conflict of interest.

Author Contributions

J.M. conceived the idea, designed and performed the experiments. J.S. and T.H. conducted theoretical calculation, data visualization, and analysis. J.M. performed material characterizations, data processing, analysis, and visualization. D.Q. performed the synchrotron characterization and data analysis. L.K., T.L., and A.D. provided the computing resources and involved into the discussions. J.M. wrote the manuscript. Z.S. performed analysis and revised the manuscript.

Data Availability Statement

Research data are not shared.

Keywords

[1] J. Mei, T. Liao, Z. Sun, *Energy Environ. Mater.* **2022**, *5*, 115.
[2] A. Mavrič, M. Fanetti, Y. Lin, M. Valant, C. Cui, *ACS Catal.* **2020**, *10*, 9451.
[3] Y. Chen, K. Rui, J. Zhu, S. X. Dou, W. Sun, *Chem. - Eur. J.* **2019**, *25*, 703.
[4] S. J. Patil, N. R. Chodankar, S.-K. Hwang, G. S. R. Raju, Y.-S. Huh, Y.-K. Han, *Small* **2022**, *18*, 2103326.
[5] C. Luan, G. Liu, Y. Liu, L. Yu, Y. Wang, Y. Xiao, H. Qiao, X. Dai, X. Zhang, *ACS Nano* **2018**, *12*, 3875.
[6] X. Kong, C. Zhang, S. Y. Hwang, Q. Chen, Z. Peng, *Small* **2017**, *13*, 1700334.
[7] M. Gao, W. Sheng, Z. Zhuang, Q. Fang, S. Gu, J. Jiang, Y. Yan, *J. Am. Chem. Soc.* **2014**, *136*, 7077.
[8] G. Zhao, P. Li, N. Cheng, S. X. Dou, W. Sun, *Adv. Mater.* **2020**, *32*, 2000872.
[9] L. Dai, Z.-N. Chen, L. Li, P. Yin, Z. Liu, H. Zhang, *Adv. Mater.* **2020**, *32*, 1906915.
[10] D. Zhu, J. Liu, L. Wang, Y. Du, Y. Zheng, K. Davey, S. Z. Qiao, *Nanoscale* **2019**, *11*, 3599.
[11] C. Kuai, C. Xi, A. Hu, Y. Zhang, Z. Xu, D. Nordlund, C.-J. Sun, C. A. Cadigan, R. M. Richards, L. Li, C.-K. Dong, X.-W. Du, F. Lin, *J. Am. Chem. Soc.* **2021**, *143*, 18519.
[12] L. J. Enman, M. S. Burke, A. S. Batchellor, S. W. Boettcher, *ACS Catal.* **2016**, *6*, 2416.
[13] X. Qiao, H. Kang, Y. Li, K. Cui, X. Jia, H. Liu, W. Qin, M. Pupucevski, G. Wu, *ACS Appl. Mater. Interfaces* **2020**, *12*, 36208.
[14] K. Yan, M. Sheng, X. Sun, C. Song, Z. Cao, Y. Sun, *ACS Appl. Energy Mater.* **2019**, *2*, 1961.
[15] T. Kou, S. Wang, J. L. Hauser, M. Chen, S. R. J. Oliver, Y. Ye, J. Guo, Y. Li, *ACS Energy Lett.* **2019**, *4*, 622.
[16] J. Jiang, F. Sun, S. Zhou, W. Hu, H. Zhang, J. Dong, Z. Jiang, J. Zhao, J. Li, W. Yan, M. Wang, *Nat. Commun.* **2018**, *9*, 2885.
[17] J. Yan, L. Kong, Y. Ji, J. White, Y. Li, J. Zhang, P. An, S. Liu, S. T. Lee, T. Ma, *Nat. Commun.* **2019**, *10*, 2149.
[18] Q. He, Y. Wan, H. Jiang, Z. Pan, C. Wu, M. Wang, X. Wu, B. Ye, P. M. Ajayan, L. Song, *ACS Energy Lett.* **2018**, *3*, 1373.
[19] X. P. Wang, H. J. Wu, S. B. Xi, W. S. V. Lee, J. Zhang, Z. H. Wu, J. O. Wang, T. D. Hu, L. M. Liu, Y. Han, S. W. Chee, S. C. Ning, U. Mirsaidov, Z. B. Wang, Y. W. Zhang, A. Borgna, J. Wang, Y. H. Du, Z. G. Yu, S. J. Pennycook, J. M. Xue, *Energy Environ. Sci.* **2020**, *13*, 229.
[20] N. Kim, D. Lim, Y. Choi, S. E. Shim, S. H. Baeck, *Electrochim. Acta* **2019**, *324*, 134868.
[21] W. Lei, G. Liu, J. Zhang, M. Liu, *Chem. Soc. Rev.* **2017**, *46*, 3492.
[22] H. Liu, K. Hu, D. Yan, R. Chen, Y. Zou, H. Liu, S. Wang, *Adv. Mater.* **2018**, *30*, 1800295.
[23] J. Pang, A. Bachmatiuk, Y. Yin, B. Trzebicka, L. Zhao, L. Fu, R. G. Mendes, T. Gemming, Z. Liu, M. H. Rummeli, *Adv. Energy Mater.* **2018**, *8*, 1702093.
[24] Y. Sui, J. Zhou, X. Wang, L. Wu, S. Zhong, Y. Li, *Mater. Today* **2020**, *42*, 117.
[25] X. Ren, J. Zhou, X. Qi, Y. Liu, Z. Huang, Z. Li, Y. Ge, S. C. Dhanabalan, J. S. Ponraj, S. Wang, J. Zhong, H. Zhang, *Adv. Energy Mater.* **2017**, *7*, 1700396.
[26] J. Mei, T. He, J. Bai, D. Qi, A. Du, T. Liao, G. A. Ayoko, Y. Yamauchi, L. Sun, Z. Sun, *Adv. Mater.* **2021**, *33*, 2104638.
[27] Z. Yuan, J. Li, M. Yang, Z. Fang, J. Jian, D. Yu, X. Chen, L. Dai, *J. Am. Chem. Soc.* **2019**, *141*, 4972.
[28] X. Wang, R. K. M. Raghupathy, C. J. Querebillo, Z. Liao, D. Li, K. Lin, M. Hantusch, Z. Sofer, B. Li, E. Zschech, I. M. Weidinger, T. D. Kühne, H. Mirhosseini, M. Yu, X. Feng, *Adv. Mater.* **2021**, *33*, 2008752.
[29] J. J. Wang, D. Liu, H. Huang, N. Yang, B. Yu, M. Wen, X. Wang, P. K. Chu, X.-F. F. Yu, *Angew. Chem.* **2018**, *130*, 2630.
[30] B. Liu, X. Li, L. Xiao, L. Zhou, Q. Xu, J. Weng, J. Xu, *Angew. Chem., Int. Ed.* **2020**, *59*, 21106.
[31] H. Chen, J. Chen, P. Ning, X. Chen, J. Liang, X. Yao, D. Chen, L. Qin, Y. Huang, Z. Wen, *ACS Nano* **2021**, *15*, 12418.
[32] F. Shi, Z. Geng, K. Huang, Q. Liang, Y. Zhang, Y. Sun, J. Cao, S. Feng, *Adv. Sci.* **2018**, *5*, 1800575.
[33] H. Qiao, H. Liu, Z. Huang, Q. Ma, S. Luo, J. Li, Y. Liu, J. Zhong, X. Qi, *Adv. Energy Mater.* **2020**, *10*, 2002424.
[34] J. Mei, T. He, Q. Zhang, T. Liao, A. Du, G. Ayoko, Z. Sun, G. A. Ayoko, Z. Sun, *ACS Appl. Mater. Interfaces* **2020**, *12*, 21720.
[35] Z. Wu, X. L. Huang, Z. L. Wang, J. J. Xu, H. G. Wang, X. B. Zhang, *Sci. Rep.* **2014**, *4*, 3669.
[36] H. Wang, X. Yang, W. Shao, S. Chen, J. Xie, X. Zhang, J. Wang, Y. Xie, *J. Am. Chem. Soc.* **2015**, *137*, 11376.
[37] D. S. Hall, D. J. Lockwood, C. Bock, B. R. MacDougall, *Proc. R. Soc. A* **2015**, *471*, 20140792.
[38] J. Mei, Y. Zhang, T. Liao, X. Peng, G. A. Ayoko, Z. Sun, *Energy Storage Mater.* **2019**, *19*, 424.
[39] B. Tian, B. Tian, B. Smith, M. C. Scott, Q. Lei, R. Hua, Y. Tian, Y. Liu, *Proc. Natl. Acad. Sci* **2018**, *115*, 4345.
[40] C. Kuai, Y. Zhang, D. Wu, D. Sokaras, L. Mu, S. Spence, D. Nordlund, F. Lin, X. W. Du, *ACS Catal.* **2019**, *9*, 6027.
[41] M. Al Samarai, A. W. Hahn, A. Beheshti Askari, Y. T. Cui, K. Yamazoe, J. Miyawaki, Y. Harada, O. Rüdiger, S. Debeer, *ACS Appl. Mater. Interfaces* **2019**, *11*, 38595.
[42] H. Jin, S. Xin, C. Chuang, W. Li, H. Wang, J. Zhu, H. Xie, T. Zhang, Y. Wan, Z. Qi, W. Yan, Y.-R. R. Lu, T.-S. S. Chan, X. Wu, J. B. Goodenough, H. Ji, X. Duan, *Science* **2020**, *370*, 192.
[43] Y.-C. Zhang, C. Han, J. Gao, L. Pan, J. Wu, X.-D. Zhu, J.-J. Zou, *ACS Catal.* **2021**, *11*, 12485.
[44] R. Prasannachandran, T. V. Vineesh, A. Anil, B. M. Krishna, M. M. Shaijumon, *ACS Nano* **2018**, *12*, 11511.
[45] L. Fang, Z. Jiang, H. Xu, L. Liu, Y. guan, X. Gu, Y. Wang, *J. Catal.* **2018**, *357*, 238.
[46] H. Liang, F. Meng, M. Cabán-Acevedo, L. Li, A. Forticaux, L. Xiu, Z. Wang, S. Jin, *Nano Lett.* **2015**, *15*, 1421.
[47] X. D. Zhu, Y. Xie, Y. T. Liu, *J. Mater. Chem. A* **2018**, *6*, 21255.

[48] J. Bai, J. Mei, T. Liao, Q. Sun, Z. Chen, Z. Sun, *Adv. Energy Mater.* **2022**, *12*, 2103247.

[49] Y. Wu, J. Yang, T. Tu, W. Li, P. Zhang, Y. Zhou, J. Li, J. Li, S. Sun, *Angew. Chem., Int. Ed.* **2021**, *60*, 26829.

[50] Z. Qiu, C. W. Tai, G. A. Niklasson, T. Edvinsson, *Energy Environ. Sci.* **2019**, *12*, 572.

[51] S. Lee, L. Bai, X. Hu, *Angew. Chem., Int. Ed.* **2020**, *59*, 8072.

[52] Z. Yan, H. Sun, X. Chen, H. Liu, Y. Zhao, H. Li, W. Xie, F. Cheng, J. Chen, *Nat. Commun.* **2018**, *9*, 2373.

[53] J. Kang, X. Qiu, Q. Hu, J. Zhong, X. Gao, R. Huang, C. Wan, L. M. Liu, X. Duan, L. Guo, *Nat. Catal.* **2021**, *4*, 1050.

[54] S. Y. Lee, I. S. Kim, H. S. Cho, C. H. Kim, Y. K. Lee, *Appl. Catal. B Environ.* **2021**, *284*, 119729.

[55] P. W. Menezes, S. Yao, R. Beltrán-Suito, J. N. Hausmann, P. V. Menezes, M. Driess, *Angew. Chem., Int. Ed.* **2021**, *60*, 4640.

[56] S. Lee, K. Banjac, M. Lingenfelder, X. Hu, *Angew. Chem.* **2019**, *131*, 10401.

[57] B. A. Naqvi, M. A. Shehzad, J. Cha, K. A. Min, M. F. Khan, S. Hussain, Y. Seo, S. Hong, J. Eom, J. Jung, *Sci. Rep.* **2018**, *8*, 12966.

[58] P. Carbonnière, C. Pouchan, *Chem. Phys. Lett.* **2008**, *462*, 169.

[59] X. Liu, K. Ni, B. Wen, R. Guo, C. Niu, J. Meng, Q. Li, P. Wu, Y. Zhu, X. Wu, L. Mai, *ACS Energy Lett.* **2019**, *4*, 2585.

2201141 (10 of 10)